nature research

https://doi.org/10.1038/s41560-020-0668-8

Supplementary information

Diagnosing and correcting anode-free cell failure via electrolyte and morphological analysis

In the format provided by the authors and unedited

Supplementary Information

Supplementary Tables

Supplementary Table 1 | Cell parameters.

	Anode-Free		Lithium-ion	
	Positive	Negative	Positive	Negative
Material	NMC*	-	NMC*	AG†
Thickness (μm)	46.25	-	46.25	65.5
Loading (mg/cm^2)	15.7	-	15.7	9.94
Current Collector (CC)	Aluminum	Copper	Aluminum	Copper
CC Thickness (μm)	13	8	13	8
	Cell		Cell	
Stack Mass (mg/cm^2)	43.82		64.31	
Stack Thickness (μm)	167		272.5	
Average Voltage	3.9		3.7	
Stack Energy (Wh)	0.89		0.85	
Stack Volumetric Energy Density (Wh/L)	1231		720	
Stack Specific Energy Density (Wh/kg)	469		305	

*$Li[Ni_{0.5}Mn_{0.3}Co_{0.2}]O_2$
†Artificial graphite

Supplementary Figures

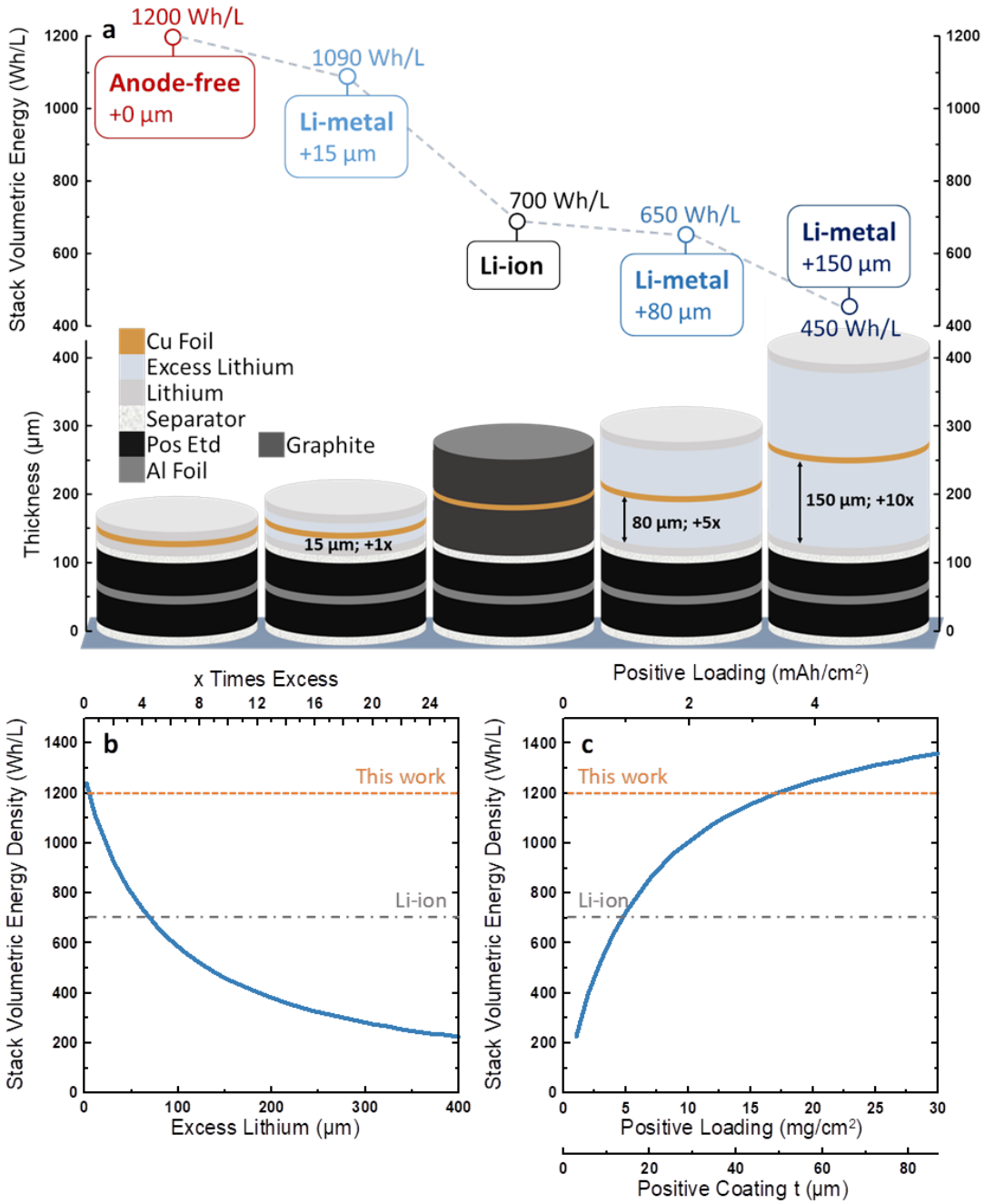

Supplementary Fig. 1 | Energy density dependence on cell parameters. a, Energy density for cell stacks with different amounts of excess lithium (top) and their respective stack diagrams (bottom). **b**, Stack energy density vs excess lithium in µm (bottom axis) and as x times excess (top axis). **c**, Stack energy density vs positive electrode coating thickness (bottom axis), positive electrode loading (middle axis) and positive electrode areal capacity (top axis). The source data for panels **b** and **c** are available in the Supplementary Data file.

Supplementary Fig. 1 explores how the stack energy density of lithium metal cells is affected by excess lithium and positive electrode loading. All other cell stack parameters used for these calculations are the same as shown in in **Supplementary Table 1**. **Fig. 1a** shows the energy density for several cell designs with excess lithium, compared to anode-free with zero (0 μm) excess lithium and a Li-ion cell. Stack diagrams for each of these cells are illustrated at the bottom of **Supplementary Fig. 1a**. **Supplementary Fig. 1b** shows the energy density as a function of excess lithium shown as both thickness (bottom axis) and how many times excess capacity that thickness corresponds to (top axis). For zero excess lithium, the energy density is ca. 1200 Wh/L. Lithium foils used in lithium metal cells in the literature range in thickness from 150-400 μm, corresponding to 10-25x excess lithium and resulting paltry energy densities of 460 and 220 Wh/L, significantly lower than lithium-ion cells. To achieve Li-ion parity, lithium excess must be limited to less than 60 μm or 4.5x excess. Limiting excess to 30 μm as suggested by Albertus et al.,[1] corresponding to 2x excess, yields an energy density of 940 Wh/L.

Supplementary Fig. 1c shows the dependence of stack energy density on positive electrode loading. In this work, cells with had a positive electrode loading of 15.7 mg/cm^2, corresponding to a coating thickness of 46.25 μm and an areal capacity of 3.1 mAh/μm. This results in a stack energy density of ca. 1200 Wh/L. Adjusting the coating thickness would change the loading, areal capacity and resulting energy density. To achieve Li-ion parity, the positive electrode loading must exceed 5 mg/cm^2, and an areal capacity of 1 mAh/cm^2, at a minimum, must be cycled. It is sometimes claimed that high areal capacities of >4 mAh/cm^2 must be achieved. However, our analysis shows that increasing areal capacity to 4 and even 5 mAh/ cm^2 increases the energy density by 50 and 100 Wh/L, or only 4 and 8% higher than the cells exhibited in this work.

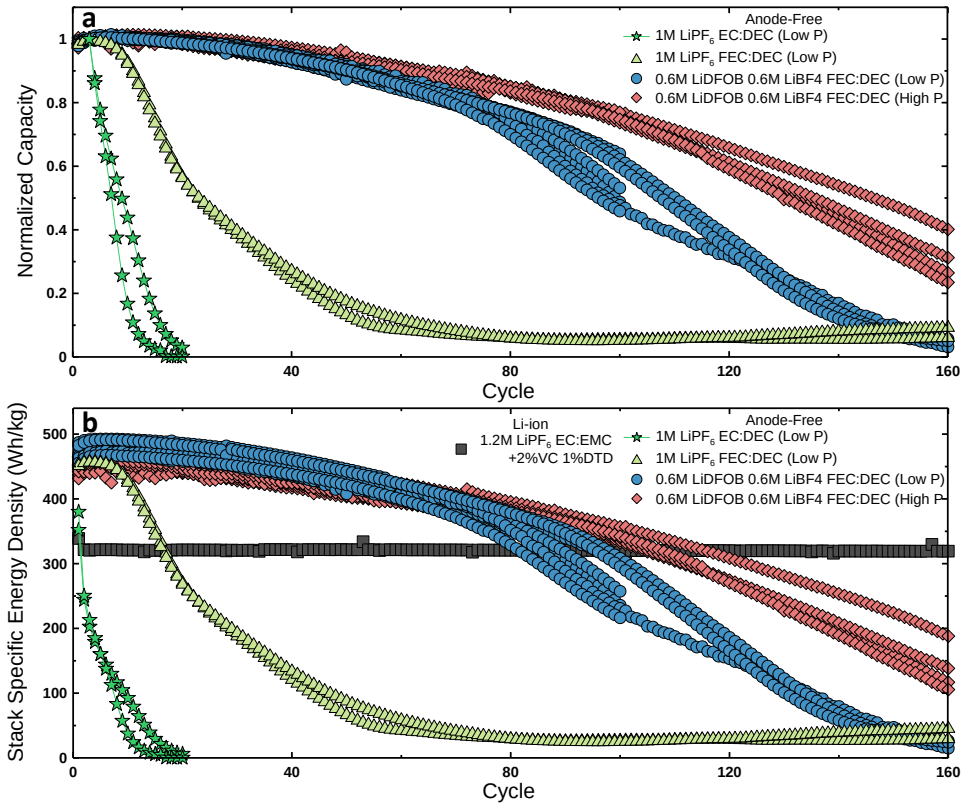

Supplementary Fig. 2 | Normalized capacity and specific energy density. a, Normalized capacity and **b,** Stack specific energy density vs cycle for anode-free cells with different electrolytes compared to an optimized Li-ion chemistry. Cells were cycled at C/5 and D/2 current rates between 3.6-4.5 V at 40ºC. Low pressure = "Low P" = 170 kPa; high pressure = "High P" = 1170 kPa. The source data for these plots are available in the Supplementary Data file.

Supplementary Fig. 2 shows the normalized capacity and specific energy density vs cycle number of anode-free cells with different electrolytes compared to an optimized Li-ion chemistry. Primitive electrolytes using 1 M LiPF6 salt in EC:DEC or FEC:DEC solvents fall below 80% capacity retention and below the specific energy density delivered by a lithium-ion cell quickly in under 20 cycles. Dual-salt 0.6 M 0.6 M LiBF4 FEC:DEC electrolyte cells sustain 80 and 90 cycles to 80% capacity under low and high pressure, respectively. The dual-salt electrolyte enables anode-free cells which deliver a specific energy density greater than Li-ion (> 300 Wh/kg) for 100 and 120 cycles when operated under low and high pressure, respectively.

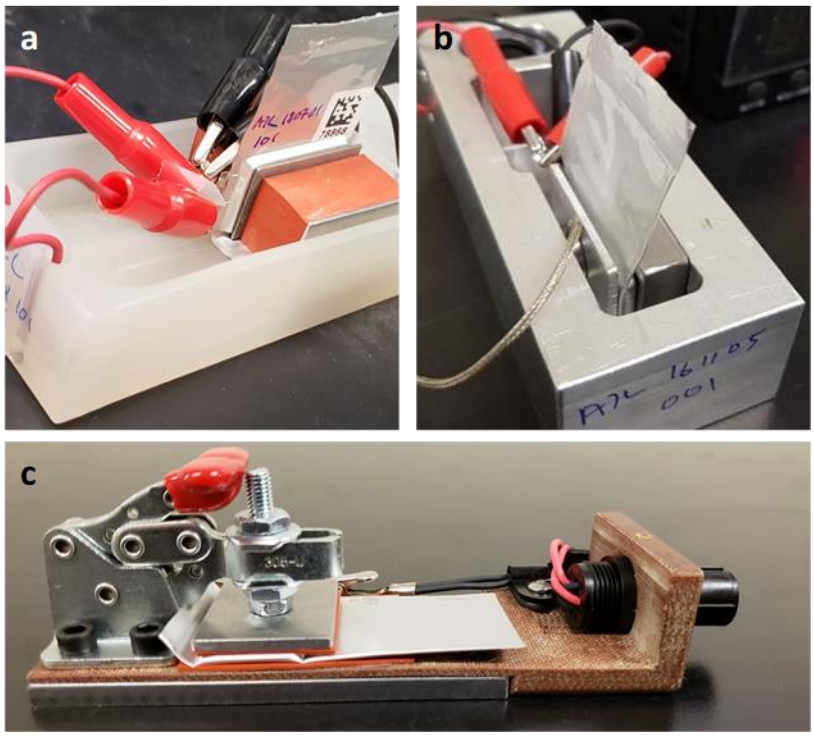

Supplementary Fig. 3 | Cell constraining fixtures. a, A plastic fixture which constrains cells under low pressure (170 kPa) using rubber blocks. **b,** An aluminum fixture with an adjustable wall allowing for the applied pressure to be controlled. **c,** A fixture which applies high uniaxial stack pressure (1170 kPa) via clamping with a DESTACO clamp.

Supplementary Fig. 3 shows the different cell fixtures used to apply uniaxial stack pressure to pouch cells in this work. **Supplementary Fig. 3a** shows a plastic enclosure in which a cell is clamped with rubber blocks to apply a pressure of ~170 kPa. Cells cycled in this type of fixture are said to be tested under "low pressure" in this work. **Supplementary Fig. 3b** shows an analogous fixture but made from aluminum. This design has previously been described.[2,3] This fixture has an adjustable wall that allows the applied pressure to be controlled by tightening screws. A pressure sensor is inserted into the fixture to measure the applied pressure. **Supplementary Fig. 3c** shows the fixture used to apply "high pressure" to cells tested in this work. A DESTACO clamp is used to constrain cells at ~1170 kPa. It is likely that the pressure distribution over the jelly roll is not completely uniform in these testing fixtures. The low pressure fixture may result in lower pressure towards the top of the jelly roll since the fixture walls do not extend all the way to the top of the jelly roll. The high pressure fixture may result in a higher pressure towards the center of the jelly roll

where it is the thickest due to the electrode tabs. Therefore, the lithium morphology may be systematically more compact in these higher pressure regions.

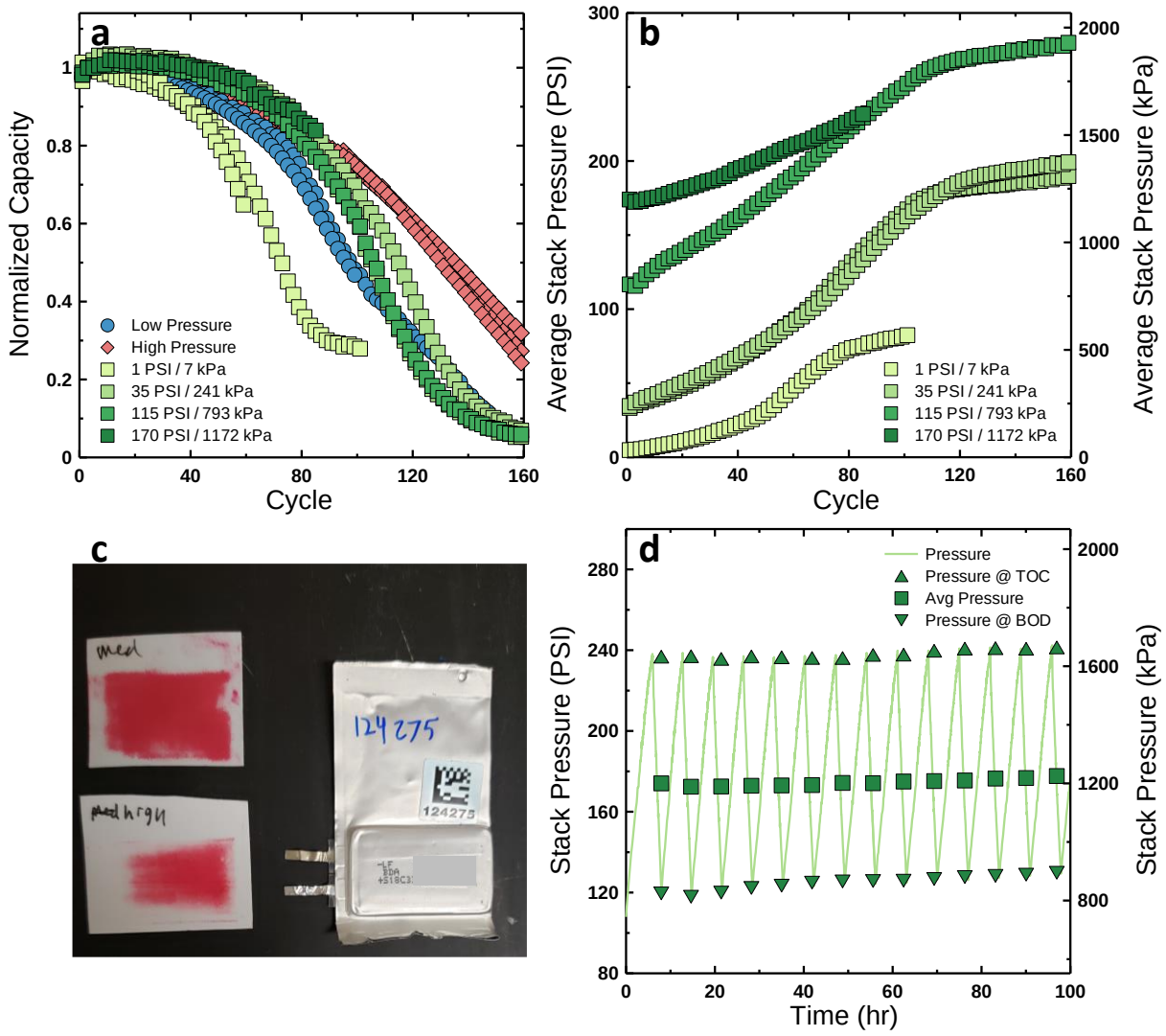

Supplementary Fig. 4 | Impact of pressure. a, Capacity retention of cells constrained under different pressures. **b,** Average stack pressure of cells cycled in the fixture shown in **Supplementary Fig. 3b**. **c,** Picture of 600 kPa (top) and 1500 kPa (bottom) pressure paper and the pouch cell the paper was constrained with in the fixture shown in **Supplementary Fig. 3c**. **c,** Stack pressure vs time of a cell cycled the fixture shown in **Supplementary Fig. 3b**.

Supplementary Fig. 4a shows the capacity retention of cells with dual-salt electrolyte cycled under different pressure constraints. Cells labeled "low pressure" and "high pressure" were cycled in fixtures shown in **Supplementary Fig. 3a** and **c**, respectively. Cells were also cycled in a variable pressure fixture shown in **Supplementary Fig. 3b** which has an adjustable wall that can be tightened to control the pressure

applied. This was done to measure the impact of pressure on cell performance. We have previously studied this with anode-free cells containing $LiPF_6$ electrolyte.[3] Cells constrained under high pressure (1170 kPa) perform better than cells under low pressure (170 kPa). When cells were cycled in the variable pressure fixture at 7 kPa, the performance was worse than with the low pressure fixture. At 241 kPa, the performance was analogous to the low pressure condition, and this was not improved at 793 kPa. When the variable pressure fixture was set to 1171 kPa, the performance tracked cells constrained in the high pressure fixtures.

When cells are constrained in non-compliant fixtures such as in **Supplementary Figs. 3b** and **3c**, the stack pressure will not remain constant. During each cycle, the pressure will increase during charge when lithium plating increases the thickness of the electrode stack, and then decrease again during discharge. To quantify the pressure during any given cycle, one can determine the maximum pressure at the top of charge, the minimum pressure at the bottom of discharge, and the average pressure. This is shown in **Supplementary Fig. 4d**. This reversible pressure change is accompanied by an irreversible pressure growth that develops during cycling due to the accumulation of SEI and dead lithium.[3] The increase in average pressure vs cycle for cells cycled in the variable pressure fixtures with inserted pressure sensors is shown in **Supplementary Fig. 4b**.

To determine the stack pressure applied by the DESTACO clamp fixture shown in **Supplementary Fig. 3c**, a cell was cycled in this fixture with pressure paper placed between the jelly roll and the clamp face. A picture of this pressure paper test is shown in **Supplementary Fig. 4c**. Two grades of pressure paper were used: one that saturates at 600 kPa (top) and one that saturates at 1500 kPa (bottom). The 600 kPa capacity pressure paper was completely saturated, while the 1500 kPa pressure paper was partially activated.

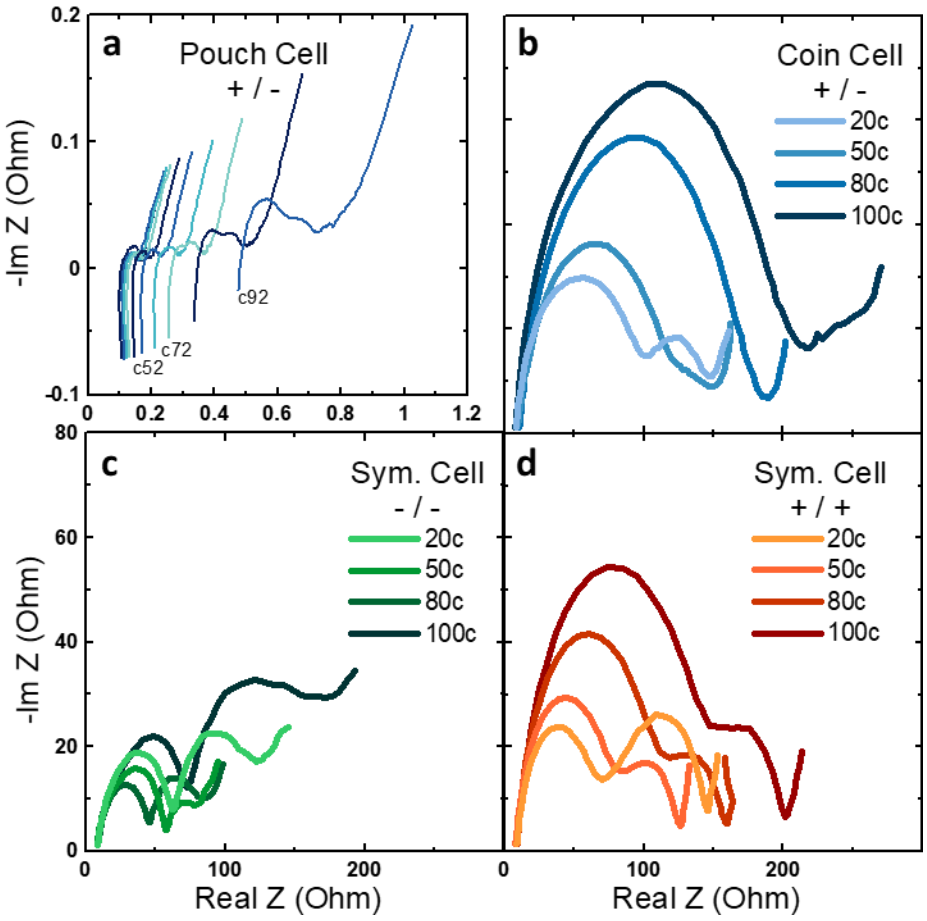

Supplementary Fig. 5 | Impedance growth. a, In-situ impedance of pouch cells during cycling using an FRA system. **b,** Ex-situ impedance of a coin cell made with harvested electrodes from pouch cells that had cycled 20, 50, 80 and 100 times. **c-d** Ex-situ impedance of negative-negative and positive-positive symmetric cells made with harvested electrodes from cycled pouch cells.

Supplementary Fig. 5 shows the Nyquist impedance growth of cells with dual-salt electrolyte. **Supplementary Fig. 5a** shows in-situ impedance measurements performed on pouch cells constrained under low pressure cycled on a Frequency Response Analyzer (FRA) system.[4] The charge transfer resistance (R_{ct}) and solution resistance (R_e) are determined by measuring the Nyquist diameter and the Real Z shift from zero, respectively.[5] The tabulated R_e, R_{ct} and total resistance $R_e + R_{ct}$ are shown in **Fig. 3c**.

To deconvolute the R_{ct} impedance contributions of the positive and negative electrodes, symmetric coin cells were made from electrodes harvested from cycled pouch cells and their impedance was measured ex-situ after 20, 50, 80 and 100 cycles. Impedance measurements were also made on positive-negative "full"

coin cells for comparison. **Supplementary Fig. 5b** shows the full cell impedance evolution. Since these measurements were performed ex-situ, information about change in R_e is lost—only the change of R_{ct} can be tracked. **Supplementary Fig. 5b** shows that through 50 cycles, the full cell R_{ct} remains relatively stable, in agreement with the FRA measurements shown in **Supplementary Fig. 5a**. **Supplementary Fig. 5c** shows the negative-negative symmetric cell impedance. The R_{ct} remains stable through most of the cycling, only showing large growth after 100 cycles. In contrast, **Supplementary Fig. 5d** shows that the positive-positive symmetric cells exhibit R_{ct} growth all throughout cycling. It is possible that the growth in impedance shown here may be due to increased contact impedance which typically manifests as the high frequency semi-circle in Nyquist plots.[6] Further work is required to fully understand the underlying mechanism of the positive-positive symmetric cell impedance growth.

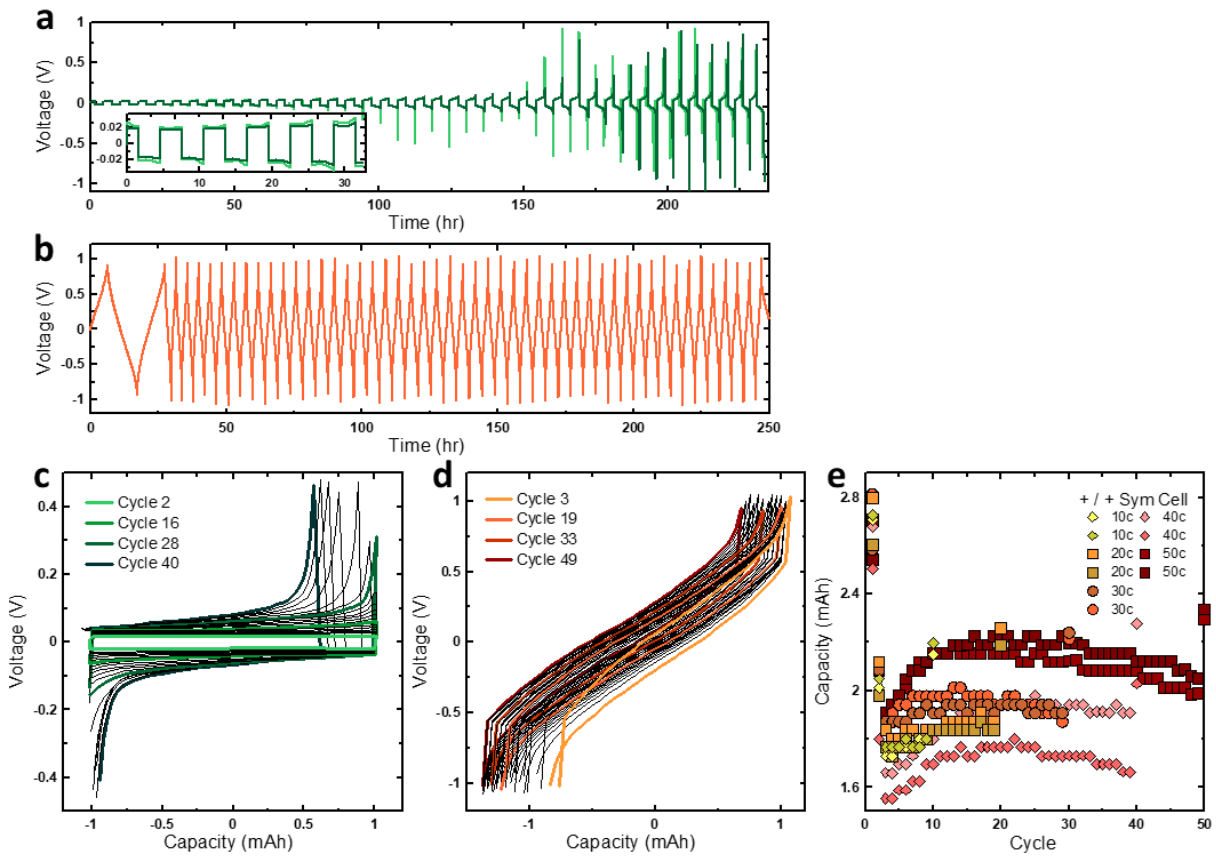

Supplementary Fig. 6 | Dual-salt symmetric cell cycling. a-b, Voltage vs time of lithium-lithium and positive-positive symmetric cells with dual-salt electrolyte. **c-d**, Voltage vs capacity of lithium-lithium and positive-positive symmetric cells. **e**, Capacity vs cycle of positive-positive symmetric cells. Positive symmetric cells were cycled to reach 4.5 V vs Li.

Symmetric coin cells were built from electrodes harvested from pouch cells after being charged once and then discharged to 50% SOC. Symmetric cells were cycled and then their electrolyte was extracted for NMR analysis shown in **Fig. 3**. **Supplementary Fig. 6** shows the electrochemical data for symmetric cells cycled with dual-salt electrolyte. Negative-negative symmetric cells were cycled to a fixed capacity of 2.028 mAh. Positive-positive symmetric cells were cycled between -0.92-0.92 V. This voltage range is equivalent to cycling the positive electrodes to potential of 4.5 V vs. Li. The voltage vs time and voltage vs capacity data for these cells are shown in **Supplementary Fig. 6a-d**. The capacity vs cycle data for positive-positive symmetric cells are shown in **Supplementary Fig. 6e**. Positive-positive symmetric cells were also cycled between -0.7-0.7 V to achieve a voltage vs Li of 4.3 V (**Supplementary Fig. 7**).

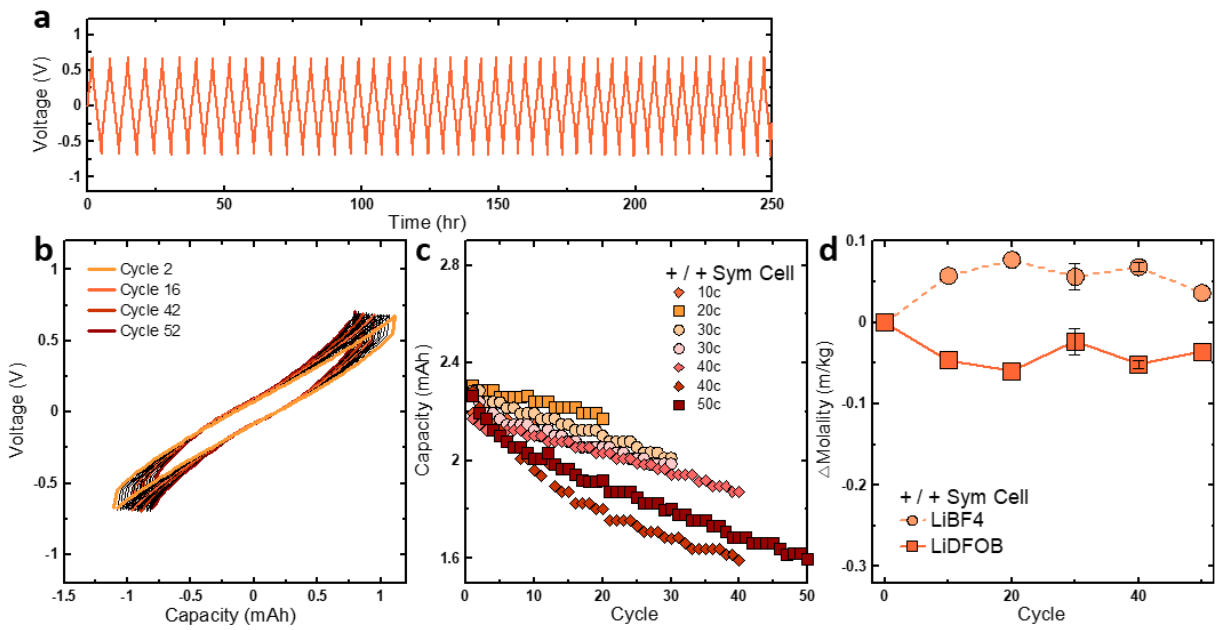

Supplementary Fig. 7 | Low voltage positive symmetric cell cycling. a, Voltage vs time of positive-positive symmetric cells with dual-salt electrolyte. **b**, Voltage vs capacity of positive-positive symmetric cells. **c**, Capacity vs cycle of positive-positive symmetric cells. **d**, Molality vs cycle of dual-salt electrolyte determined by NMR. Positive symmetric cells were cycled to reach 4.3 V vs Li.

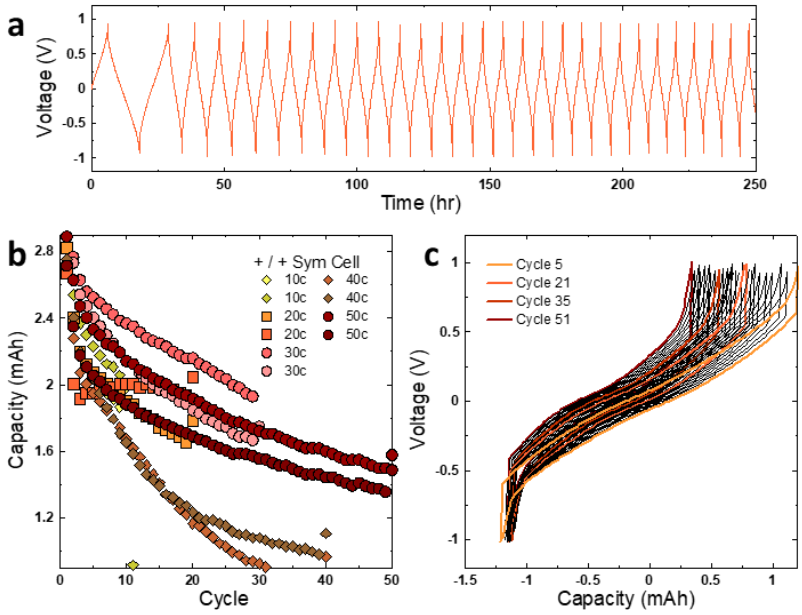

Supplementary Fig. 8 | Single-salt positive symmetric cell cycling. a, Voltage vs time of positive-positive symmetric cells with single-salt electrolyte. **b**, Capacity vs cycle of positive-positive symmetric cells. **b**, Voltage vs capacity of positive-positive symmetric cells. Positive symmetric cells were cycled to reach 4.5 V vs Li.

The electrochemical data for positive-positive symmetric cells built with single-salt LiDFOB electrolyte are shown in **Supplementary Fig. 8**. Cells were cycled between -0.92-0.92 V to achieve a voltage vs Li. of 4.5 V. The voltage vs time and voltage capacity data are shown in **Supplementary Fig. 8a** and **c**. The capacity vs cycle data are shown in **Supplementary Fig. 8b**.

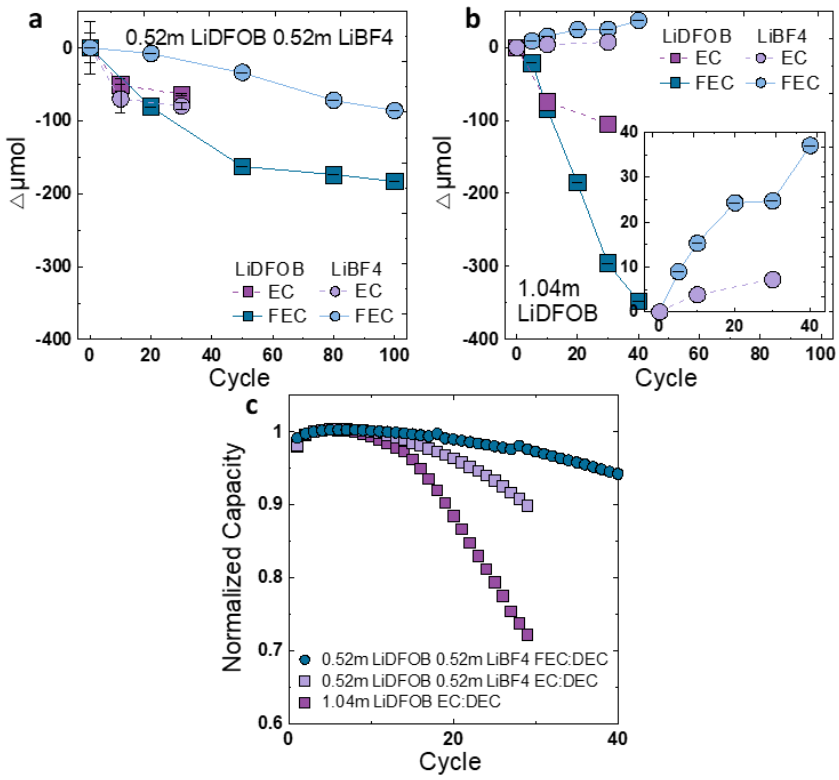

Supplementary Fig. 9 | FEC-free electrolyte test. a-b, Change in µmol of LiDFOB and $LiBF_4$ salt in dual-salt (a) and single-salt cells (b). Data for cells using FEC:DEC solvent are shown in blue (solid lines), and cells using EC:DEC solvent are shown in purple (dashed lines). **c**, Capacity vs cycle of normal dual-salt cells, dual-salt cells with EC:DEC solvent and single salt-cells with EC:DEC solvent. Cycling was performed at C/5 and D/2 between 3.6-4.5 V at 40ºC and under low pressure.

To test the impact of FEC-containing solvent on the performance of dual- and single-salt electrolyte and the consumption of LiDFOB and $LiBF_4$, pouch cells were tested with EC:DEC electrolyte along with the conventional FEC:DEC solvent blend. The capacity retention of these cells are shown in **Supplementary Fig. 9c**. FEC-containing cells with dual-salt perform the best. Without FEC, dual-salt cells show poor cycle life, and single-salt cells exhibit rapid capacity loss. The salt consumption of dual- and single-salt cells with FEC-free electrolyte are shown in **Supplementary Figs. 9a** and **9b**, respectively. Data for conventional FEC-containing electrolyte, shown in blue, is included for comparison. **Supplementary Fig. 9a** shows that FEC-free dual-salt cells consume LiDFOB at a similar rate to FEC-containing cells, however, $LiBF_4$ appears to be consumed more rapidly. **Supplementary Fig. 9b** shows that FEC-free single-salt cells again consume similar amounts of LiDFOB compared to FEC-containing cells for the first 10 cycles, after which

the rate of consumption decreases likely due to the significant capacity loss resulting in depletion of active lithium. The FEC-free cells do exhibit $LiBF_4$ production, but at a significantly lower rate than FEC-containing cells. This indicates that $LiBF_4$ can be consumed without the consumption of FEC but at a lower rate, suggesting a beneficial synergetic effect between the presence of FEC and $LiBF_4$ consumption in our optimized dual-salt electrolyte.

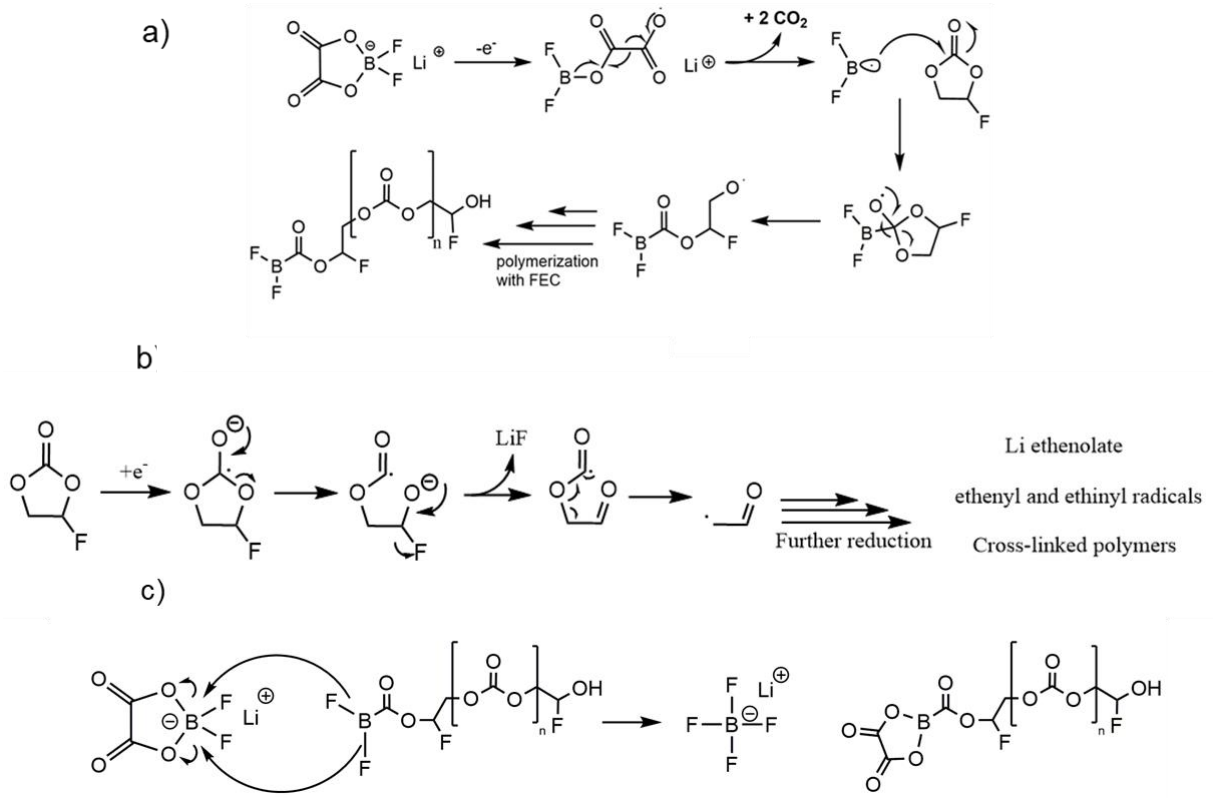

Supplementary Fig. 10 | Proposed Reaction Mechanisms. a, Oxidation reaction of LiDFOB on the positive electrode in the presence of FEC. **b**, Reduction reaction of FEC. **c**, LiDFOB reaction fluorinated boron center from **a** to produce $LiBF_4$.

Supplementary Fig. 10 shows the proposed reaction mechanism for the consumption of LiDFOB and subsequent generation of $LiBF_4$. On the positive electrode, LiDFOB can undergo an oxidative decomposition (**Supplementary Fig 10a**). This decomposition generates CO_2 and a BF_2^- radical. In the presence of FEC, the BF_2^- radical attacks the electrophilic carbonyl carbon in FEC and initiates a ring-opening reaction and subsequent polymerization which forms Li-ion conducting polymer/oligomer networks as previously reported in the presence of EC.[7] **Supplementary Fig. 10b** shows the reductive decomposition of FEC. FEC undergoes a ring-opening reaction, followed by a defluorination step to generate LiF and subsequent CO_2 release.[8] The remaining vinoxyl-radical can undergo further reduction and polymerization to generate lithium ethenolate, enthenyl and ethinyl radicals, lithium oxide and cross-linked lithium conducting polymers. Finally, **Supplementary Fig. 10c** shows that LiDFOB can undergo a fluorine-oxygen exchange with the fluorinated boron center from polymeric product in **Supplementary Fig. 10a** to generate $LiBF_4$.[9] The proposed reaction in **Supplementary Fig. 10c** is consistent with the expected increase in B-O bond dissociation enthalpies between the polymeric product in **Supplementary**

Fig. 10c and the BF_2-O bond in LiDFOB, which indicates a thermodynamically favored reaction.[10] The proposed mechanisms in **Supplementary Fig. 10** appear to be consistent with our observation and previous literature reports and provide some insight into the reactivity of our dual-salt electrolyte that can enhance the cell performance.

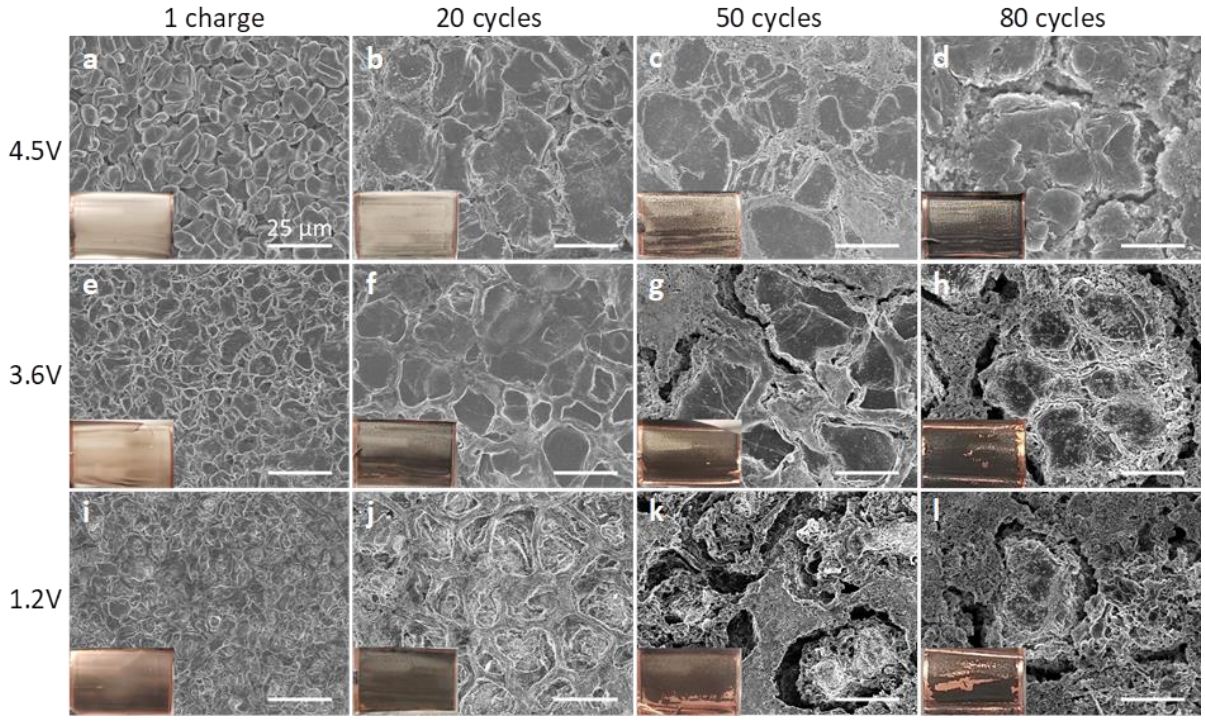

Supplementary Fig. 11 | Morphology evolution. a-d, SEM and optical images (inset) of fully plated lithium (4.5 V). **e-f**, Images after most lithium is stripped away (3.6 V). **i-l**, Images after all active lithium is stripped away after 1 charge, 20, 50 and 80 cycles. Samples were retrieved from cells cycled under low pressure.

Supplementary Fig. 11 shows the evolution of lithium morphology as a function of cycle number for cells cycled under low pressure. SEM images were taken at 3 stages of lithium plating: 100% plating at the top of charge (4.5 V, top row), after most lithium has been stripped away at the bottom of discharge (3.6 V, middle row), and after all active lithium has been stripped away (1.2 V, bottom row). The insets show optical images of the plated lithium.

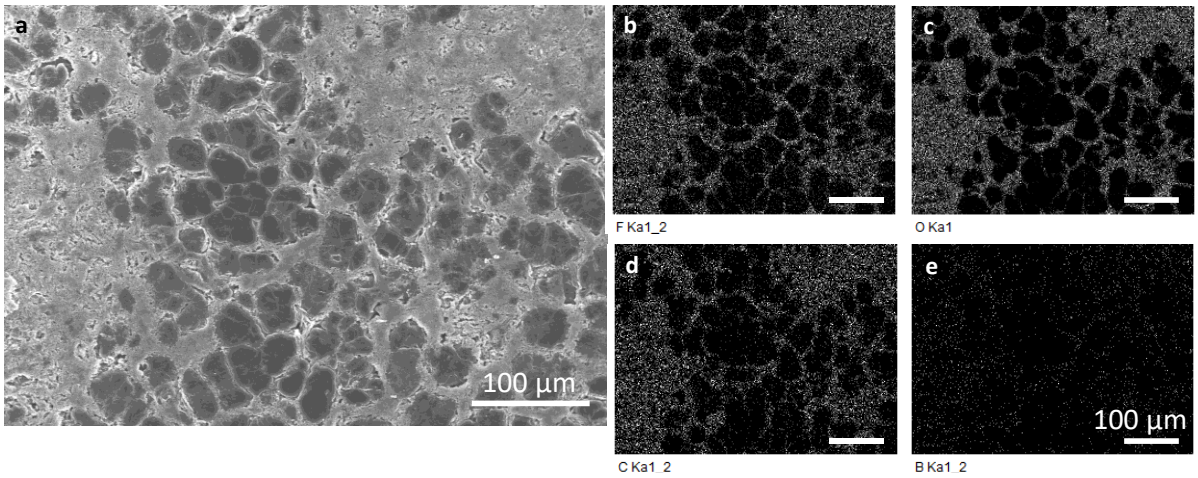

Supplementary Fig. 12 | EDS analysis. a, SEM image of plated lithium from a cell cycled with dual-salt electrolyte under high pressure after 80 cycles. **b-e**, Fluorine, oxygen, carbon and boron EDS maps.

Supplementary Fig. 12 shows energy dispersive x-ray spectroscopy (EDS) analysis of a lithium sample taken from a cell after 80 cycles constrained under high pressure. **Supplementary Fig. 12b-e** shows dot maps for fluorine, oxygen, carbon and boron, respectively. Each of these elements are expected to show up in the solid electrolyte interphase (SEI) as electrolyte decomposition products. The SEI is formed on the surface of lithium metal, therefore, a higher concentration of these decomposition products will be observed in areas with higher surface area. The dot maps show low concentration of these decomposition products on the large lithium grains. In contrast, a high concentration of these elements is observed between the lithium grains, indicating these regions exhibit high surface area.

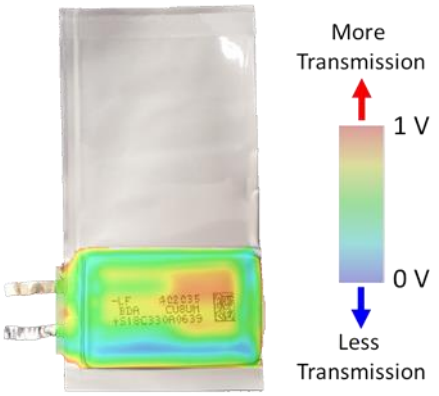

Supplementary Fig. 13 | Ultrasonic transmission map. An ultrasonic transmission map overlaid on to a picture of a pouch cell scanned in this work.

Supplementary Fig. 13 shows an ultrasonic transmission map overlaid on a pouch cell to demonstrate how the ultrasonic transmission maps shown in **Fig. 5** correspond to the pouch cells tested in this work.

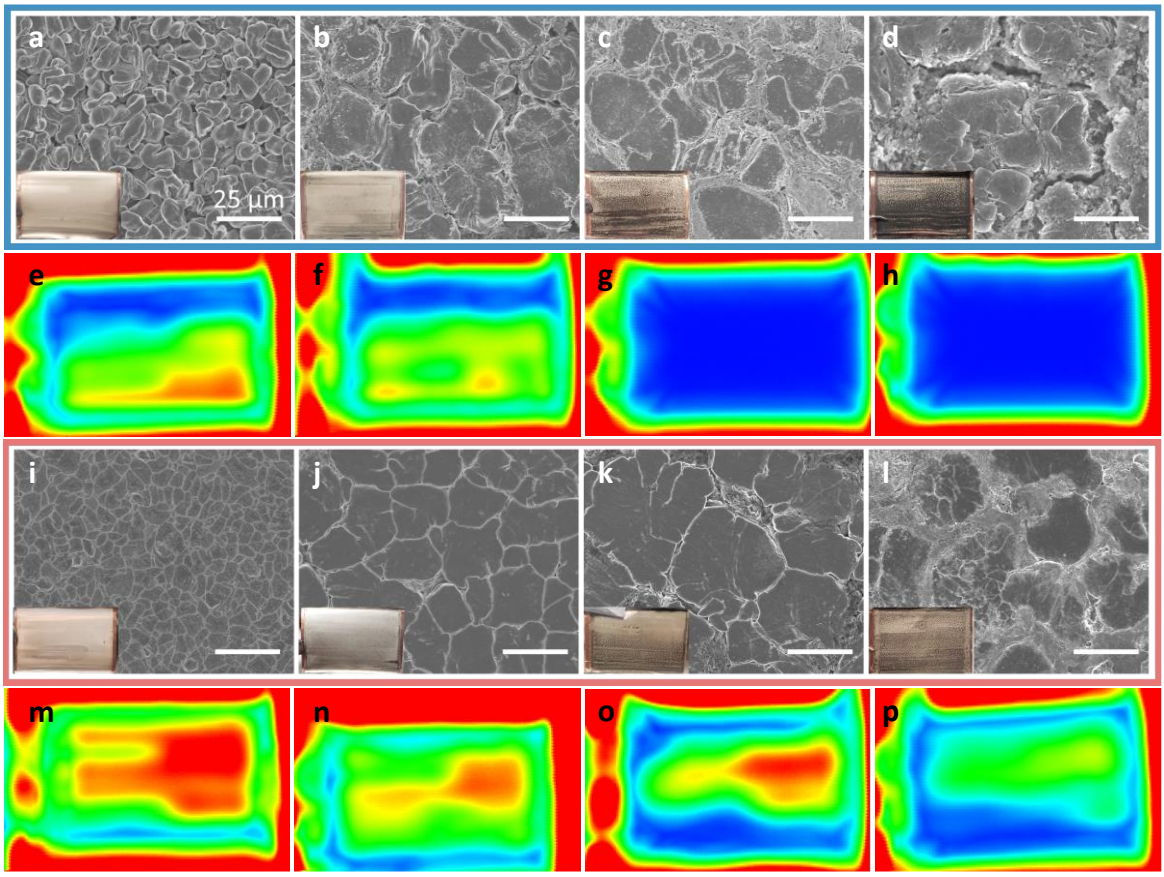

Supplementary Fig. 14 | Morphology and transmission comparison. a-d, SEM and optical images (inset) of plated lithium under low pressure. **e-f**, Ultrasonic transmission maps of cells cycled under low pressure. **i-l**, SEM and optical images (inset) of plated lithium under high pressure. **m-p**, Ultrasonic transmission maps of cells cycled under high pressure. The columns show data for cells that have charged once, 20, 50 and 80 times.

Supplementary Fig. 14 combines the morphology evolution and ultrasonic transmission maps of cells cycled under low and high pressure shown in **Fig. 1** and **Fig. 5** for comparison. **Supplementary Fig. 14a-h** show data for cells cycled under low pressure, and **Supplementary Fig. 14i-p** show data for cells cycled under high pressure. Lithium morphologies which appear more compact with less surface area exhibit ultrasonic transmission maps with higher degrees of transmission, indicating superior electrode wetting. More compact lithium morphology lessens the surface area over which the electrolyte must be distributed over, therefore this correlation between more compact morphology and higher transmission indicating superior wetting is expected.

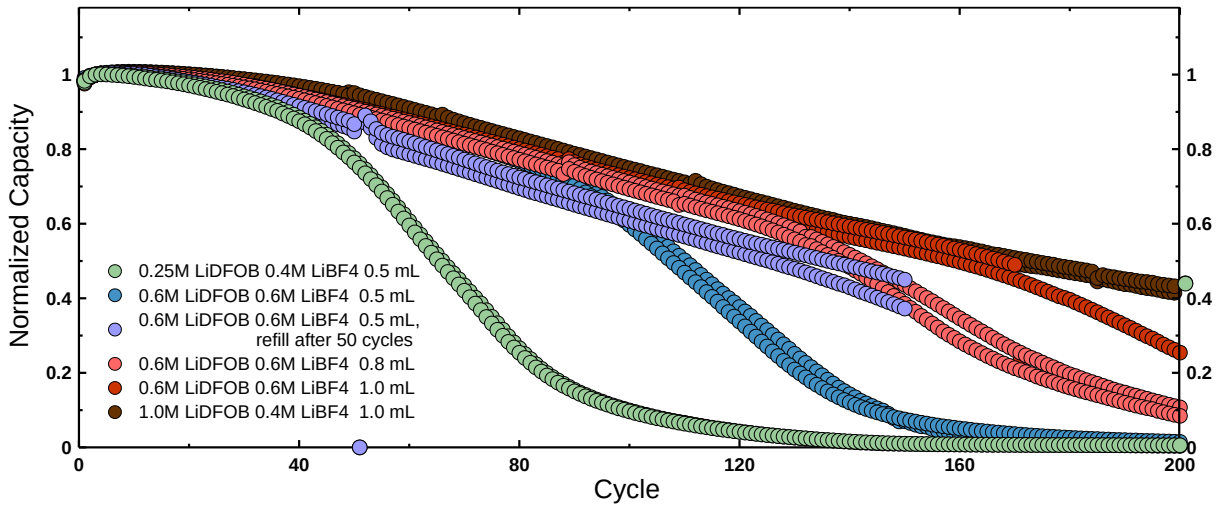

Supplementary Fig. 15 | Impact of increased electrolyte volume and concentration. Normalized capacity vs cycle for anode-free cells with varying volumes of electrolyte and concentrations of LiDFOB and LiBF4 salts. Cells were cycled at 40ºC between 3.6-4.5 V under low pressure.

Supplementary Fig. 15 shows the impact of increasing the volume of electrolyte or the concentration of salt components on the performance of anode-free cells with dual-salt electrolyte. In this work, we have shown that cells die after the depletion of the LiDFOB and $LiBF_4$ salts. Therefore, lifetime can be increased by increasing the total amount of salts present in the cell by simply increasing the volume of electrolyte. **Supplementary Fig. 15** shows how the lifetime increases by increasing the electrolyte volume above the standard 0.5 mL to 0.8 mL and 1.0 mL using the normal dual-salt recipe of 0.6 M LiDFOB + 0.6 M $LiBF_4$. Similarly, instead of initially filling with more electrolyte, **Supplementary Fig. 15** includes a test in which cells cycled for 50 times with the standard 0.5 mL of electrolyte and then were filled a further 0.5 mL of electrolyte. These cells sustained a similar lifetime to those initially filled with 1.0 mL of electrolyte.

Conversely, cell failure will be accelerated when less LiDFOB and $LiBF_4$ salt is present within the cell. This is observed in **Supplementary Fig. 15** with cells which used a lower concentration dual-salt formulation of 0.25 M LiDFOB + 0.4 M $LiBF_4$. Finally, if both the volume and concentration of electrolyte is increased, the lifetime will be extended the most, as shown with the cells filled with 1.0 mL of 1.0 M LiDFOB + 0.4 M $LiBF_4$.

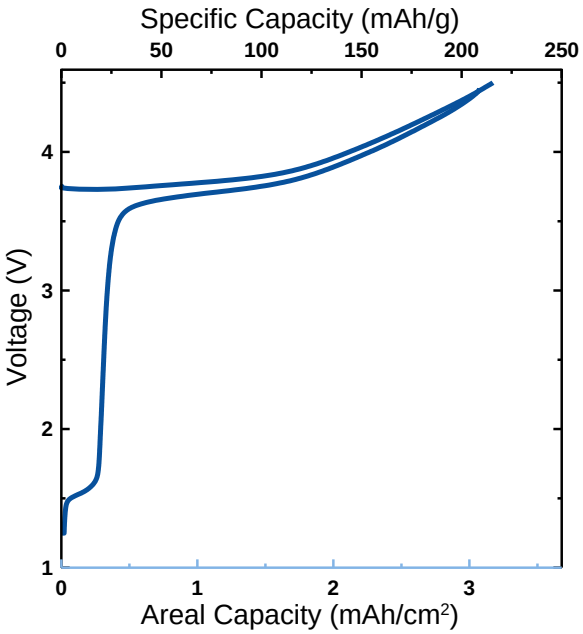

Supplementary Fig. 16 | First charge-discharge voltage curve. Voltage vs areal capacity (bottom axis) and specific capacity (top axis) of a NMC532||Cu anode-free cell used in this work. This cell was cycled at 40ºC between 1.25-4.5 V under low pressure.

Supplementary Fig. 16 shows the very first charge followed by a deep discharge to 1.25 V of an NMC532||Cu anode-free cell used in this work. Since cells in this work were cycled to a lower cutoff voltage of 3.6 V, **Supplementary Fig. 16** shows there is a ~0.5 mAh/cm^2 or 30 mAh/g cathode "irreversible capacity". The term "irreversible capacity" generally refers to the capacity that cannot be reintercalated in to the cathode after the first charge (irreversible capacities of 10s of mAh/g are common for NMC materials). However, Muller-Neuhaus et al.[11] demonstrated that this capacity is not actually lost or "irreversible", but merely impeded due to slow kinetics in Li_xMO_2 materials as $x \rightarrow 1$ and can in fact be recovered during a deep discharge, as shown in **Supplementary Fig. 16**. Therefore, during normal cycling to a lower cutoff voltage of 3.6 V, the ~0.5 mAh/cm^2 "irreversible" capacity remains plated on the copper current collector as a small ~2 µm thick lithium reservoir.

Supplementary References

1. Albertus, P., Babinec, S., Litzelman, S. & Newman, A. Status and challenges in enabling the lithium metal electrode for high-energy and low-cost rechargeable batteries. *Nat. Energy* **3**, 16–21 (2018).
2. Louli, A. J., Li, J., Trussler, S., Fell, C. R. & Dahn, J. R. Volume, Pressure and Thickness Evolution of Li-Ion Pouch Cells with Silicon-Composite Negative Electrodes. *J. Electrochem. Soc.* **164**, A2689–A2696 (2017).
3. Louli, A. J. *et al.* Exploring the Impact of Mechanical Pressure on the Performance of Anode-Free Lithium Metal Cells. *J. Electrochem. Soc.* **166**, A1291–A1299 (2019).
4. Nelson, K. J. *et al.* Studies of the Effect of High Voltage on the Impedance and Cycling Performance of Li[Ni 0.4 Mn 0.4 Co 0.2]O 2 /Graphite Lithium-Ion Pouch Cells . *J. Electrochem. Soc.* **162**, A1046–A1054 (2015).
5. Nelson, K. STUDIES OF THE EFFECTS OF HIGH VOLTAGE ON THE PERFORMANCE AND IMPEDANCE OF LITHIUM-ION BATTERIES. (2017).
6. Keefe, A. S., Buteau, S., Hill, I. G. & Dahn, J. R. Temperature Dependent EIS Studies Separating Charge Transfer Impedance from Contact Impedance in Lithium-Ion Symmetric Cells. *J. Electrochem. Soc.* **166**, A3272–A3279 (2019).
7. Zhu, Y., Li, Y., Bettge, M. & Abraham, D. P. Positive Electrode Passivation by LiDFOB Electrolyte Additive in High-Capacity Lithium-Ion Cells. *J. Electrochem. Soc.* **159**, A2109–A2117 (2012).
8. Petibon, R. *et al.* Studies of the Capacity Fade Mechanisms of $LiCoO_2$/Si-Alloy:Graphite Cells. *J. Electrochem. Soc.* **163**, A1146–A1156 (2016).
9. Allen, J. L., Han, S. D., Boyle, P. D. & Henderson, W. A. Crystal structure and physical properties of lithium difluoro(oxalato) borate (LiDFOB or LiBF2Ox). *J. Power Sources* **196**, 9737–9742 (2011).
10. Hanson, R. K. *et al.* Bond Dissociation Energies in Simple Molecules. *Spectroscopy and Optical Diagnostics for Gases* 51–57 (2016). doi:10.1007/978-3-319-23252-2_3
11. Mueller-Neuhaus, J. R., Dunlap, R. A. & Dahn, J. R. Probing Li-Ni Cation Disorder in Li 1− x Ni 1+ x − y Al y O 2 Cathode Materials by Neutron Diffraction. *J. Electrochem. Soc.* **147**, 3598–3605 (2000).